

# Origin and stability of the charge density wave in $\text{ScV}_6\text{Sn}_6$

Yanhong Gu,<sup>1</sup> Ethan Ritz,<sup>2</sup> William R. Meier,<sup>3</sup> Avery Blockmon,<sup>1</sup>  
 Kevin Smith,<sup>1</sup> Richa Pokharel Madhogaria,<sup>3</sup> Shirin Mozaffari,<sup>3</sup>  
 David Mandrus,<sup>3,4,5</sup> Turan Birol,<sup>2</sup> and Janice L. Musfeldt<sup>1,6,\*</sup>

<sup>1</sup>*Department of Chemistry, University of Tennessee, Knoxville, Tennessee 37996, USA*

<sup>2</sup>*Department of Chemical Engineering and Materials Science,  
 University of Minnesota, Minneapolis, Minnesota 55455, USA*

<sup>3</sup>*Materials Science and Engineering Department,  
 University of Tennessee Knoxville, Knoxville, Tennessee 37996, USA*

<sup>4</sup>*Department of Physics and Astronomy,  
 University of Tennessee Knoxville, Knoxville, Tennessee 37996, USA*

<sup>5</sup>*Materials Science and Technology Division,  
 Oak Ridge National Laboratory, Oak Ridge, Tennessee 37831, USA*

<sup>6</sup>*Department of Physics and Astronomy,  
 University of Tennessee, Knoxville, Tennessee 37996, USA*

(Dated: May 3, 2023)

## Abstract

Kagomé metals are widely recognized as versatile platforms for exploring novel topological properties, unconventional electronic correlations, magnetic frustration, and superconductivity. In the  $RV_6Sn_6$  family of materials ( $R = \text{Sc, Y, Lu}$ ),  $ScV_6Sn_6$  hosts an unusual charge density wave ground state as well as structural similarities with the  $AV_3Sb_5$  system ( $A = \text{K, Cs, Rb}$ ). In this work, we combine Raman scattering spectroscopy with first-principles lattice dynamics calculations to reveal the charge density wave state in  $ScV_6Sn_6$ . In the low temperature phase, we find a five-fold splitting of the V-containing totally symmetric mode near  $240 \text{ cm}^{-1}$  suggesting that the density wave acts to mix modes of  $P6/mmm$  and  $R\bar{3}m$  symmetry - an effect that we quantify by projecting phonons of the high symmetry state onto those of the lower symmetry structure. We also test the stability of the density wave state under compression and find that both physical and chemical pressure act to quench the effect. We discuss these findings in terms of symmetry and the structure-property trends that can be unraveled in this system.

---

\* musfeldt@tennessee.edu

## INTRODUCTION

Kagomé materials possess two-dimensional periodic networks of corner-sharing triangles and, as a result, exhibit a high degree of geometrical frustration. This structural frustration can create Dirac cones and flat bands in the electronic band structure, as well as exotic magnetic ground states<sup>1–8</sup> accompanied by the anomalous Hall effect,<sup>9–12</sup> charge fractionalization,<sup>13,14</sup> chiral magnetism,<sup>15,16</sup> and strong electron correlations.<sup>17</sup> The discovery of charge density waves (CDWs) in superconducting  $AV_3Sb_5$  ( $A = K, Rb, Cs$ ) and magnetic FeGe demonstrates that CDWs can exist in both magnetic and nonmagnetic kagomé lattices across a range of electron correlations.<sup>18–20</sup> At the same time, rich phase diagrams can be obtained by tuning the frustration and electron filling in the kagomé lattice. Strong entanglements make this platform well-suited to revealing intertwined and competing states. Recently, a family of bi-layer analogs with chemical formula  $RV_6Sn_6$  ( $R = Sc, Y, Lu, Tb, Ho, Gd...$ ) has attracted attention [Fig. 1a].<sup>21</sup> These kagomé metals also host topological Dirac surface states, van Hove singularities, anisotropic magnetism, and other exciting properties.<sup>22,23</sup> That said, unlike all three  $AV_3Sb_5$  compounds, superconductivity has not been reported in  $ScV_6Sn_6$  under any temperature or pressure conditions investigated thus far,<sup>24,25</sup> possibly due to the lack of a  $\Gamma$ -centered Fermi pocket in this material.<sup>26–29</sup> Also, remarkably, only  $ScV_6Sn_6$  exhibits a three dimensional CDW, making it comparable to the  $AV_3Sb_5$ 's. Despite recent activity in this highly contemporary research area, there is much more to learn about the CDW in  $ScV_6Sn_6$  and related materials. In particular, the combination of two kagomé layers per unit cell, along with the lower symmetry wavevector of the CDW makes resolving structural details and phase transition of  $ScV_6Sn_6$  a particularly daunting task.

$ScV_6Sn_6$  is a paramagnetic metal with a first-order CDW transition at 92 K ( $T_{CDW}$ ).<sup>25,30–32</sup> The CDW primarily involves out-of-plane Sc and Sn displacements; thus far, the contribution of V centers has been neglected.<sup>25,33</sup> First-principles calculations point to lattice instabilities (soft modes) in  $ScV_6Sn_6$ <sup>33</sup> - possibly due to the small size of the  $Sc^{3+}$  radius. Experimentally, a phonon mode leads to short range order in the high temperature phase with wavevector  $(1/3, 1/3, 1/2)$ . A stable long range CDW order with wavevector  $(1/3, 1/3, 1/3)$  sets in below 92 K in the low temperature phase.<sup>31,32</sup> This type of lattice instability is not present in the

Y and Lu analogs, and there are no CDWs in these materials.<sup>33</sup> Experimental confirmation of these predictions by other probes is highly desirable. Traditionally, x-ray techniques and vibrational spectroscopy have been favored for unraveling these issues. Infrared and Raman scattering spectroscopies in particular are well-suited for exploring the microscopic aspects of local lattice distortions as well as phase and amplitude modes of a CDW. Of course, the metallic character of  $\text{ScV}_6\text{Sn}_6$  challenges this approach because the odd-symmetry infrared-active phonons are screened by the Drude contribution.<sup>34</sup> Raman scattering provides a way forward,<sup>35</sup> and it has been used to gain significant insight about the CDW in other kagomé systems<sup>36,37</sup> even though it accesses only even-symmetry features at the zone center. Compared to the  $\text{AV}_3\text{Sb}_5$  family, Raman spectroscopy can provide more information about  $\text{ScV}_6\text{Sn}_6$  because of the larger number of Raman active lattice modes in its crystal structure.

In this work, we combine temperature- and pressure-dependent Raman scattering spectroscopy of  $\text{ScV}_6\text{Sn}_6$  with complementary lattice dynamics calculations to reveal the properties of the charge density wave states in this model bi-layer kagomé metal. What distinguishes our work from prior efforts<sup>38</sup> is the quality of our single crystals with different  $R$  site substitutions, the ability to employ both temperature and pressure as tuning parameters, and our symmetry-guided strategy of projecting the high temperature phase  $P6/mmm$  phonons onto those in the low temperature CDW state to uncover their origins. We find that the  $A_{1g}$  symmetry mode near  $240\text{ cm}^{-1}$  - which involves out-of-plane V center motion - is very sensitive to the development of the CDW. For instance, even though it corresponds to a nondegenerate phonon mode, it seemingly displays five-fold splitting in the low temperature phase consistent with  $R\bar{3}m$  symmetry. We discuss this symmetry breaking in terms of mixing of nearby symmetry-appropriate and zone-folded phonons. We also demonstrate that compression at room temperature quenches the recently reported short range CDW in  $\text{ScV}_6\text{Sn}_6$  but has no effect on the Lu analog. We therefore establish that density wave stability is impacted by both physical and chemical pressure. These findings revise our understanding of how and why CDWs are stabilized in  $\text{ScV}_6\text{Sn}_6$  and related materials.



## RESULTS AND DISCUSSION

### Raman-active phonons of $\text{ScV}_6\text{Sn}_6$ at 300 K

Figure 1b summarizes the Raman scattering response of  $\text{ScV}_6\text{Sn}_6$  at room temperature. We employ a symmetry analysis, complementary lattice dynamics calculations, polarizer/analyzer combinations, and chemical substitution on the  $R$  site to assign the excitations. Overall, the eight calculated phonon frequencies (blue spheres in Fig. 1b, see Supplementary Table II) are in excellent agreement with the measured spectrum. Challenging assignments are near  $240\text{ cm}^{-1}$  where there are two candidate modes and below  $200\text{ cm}^{-1}$  where the Raman-active phonons are embedded in a series of extra peaks. The latter turn out to be rotational modes of air in the optical path. They appear in this and other measurements of  $\text{ScV}_6\text{Sn}_6$ <sup>38,39</sup> due to the low brightness of the sample. The peak near  $240\text{ cm}^{-1}$  is important in our continuing discussion. According to our lattice dynamics calculations, there are two candidates for this structure:  $E_{1g}$  and  $A_{1g}$  symmetry modes. Surprisingly, the peak can be fit

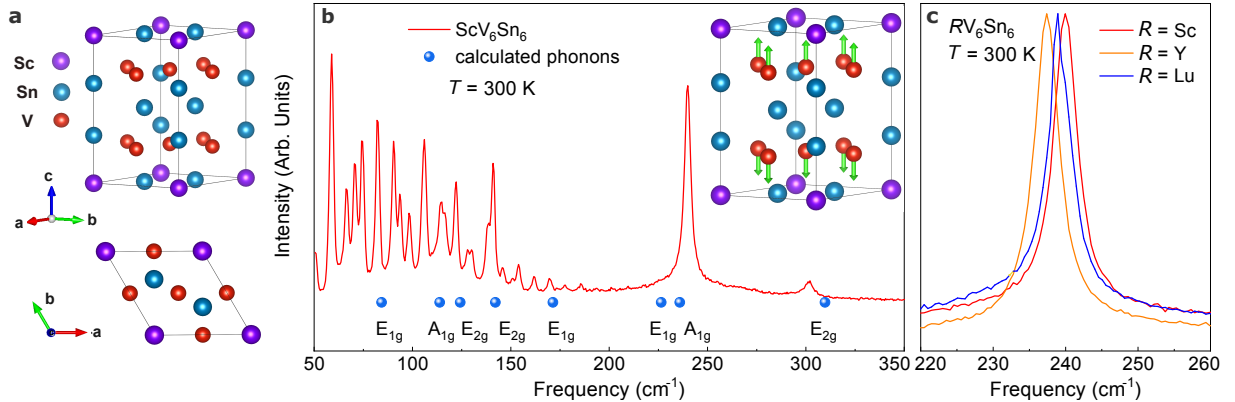


FIG. 1. **Properties of hexagonal  $\text{ScV}_6\text{Sn}_6$  at room temperature.** **a** Crystal structure of  $\text{ScV}_6\text{Sn}_6$  (space group  $P6/mmm$ , #191).<sup>25</sup> This three dimensional material hosts two vanadium kagomé layers separated by  $\text{ScSn}_2$  and  $\text{Sn}_2$  layers along the out of plane direction. **b** Raman scattering spectrum of  $\text{ScV}_6\text{Sn}_6$  compared with predictions from complementary lattice dynamics calculations. The spectrum is collected on the  $ab$  plane in the backscattering geometry. The inset shows the displacement pattern of the  $A_{1g}$  symmetry mode near  $240\text{ cm}^{-1}$ . **c** Close up view of the phonon near  $240\text{ cm}^{-1}$  in the  $RV_6\text{Sn}_6$  family materials ( $R = \text{Sc}, \text{Y}, \text{Lu}$ ).

by a single oscillator suggesting that one of these constituents is present with extremely low intensity. Based upon extinction behavior under various polarizer/analyzer arrangements [Supplementary figure 1 c], we assign the  $240\text{ cm}^{-1}$  peak as primarily an  $A_{1g}$  symmetry mode. The displacement pattern, which involves out-of-plane V center motion, is shown in the inset of Fig. 1b. Substitution on the  $R$  (Sc) site is less useful for assignment purposes because the frequency vs. mass trend is not straightforward [Fig. 1c]. The atomic radius of the  $R$  center and the precise local environment appear to be more important. The complete set of mode assignments in  $\text{ScV}_6\text{Sn}_6$  is given in Supplementary Table 1.

### Symmetry breaking across the CDW transition

Figure 2a summarizes the Raman scattering response of  $\text{ScV}_6\text{Sn}_6$  as a function of temperature in the high frequency region. We focus on the behavior of the  $A_{1g}$  symmetry mode near  $240\text{ cm}^{-1}$ . This structure hardens systematically with decreasing temperature and splits into a cluster of at least five closely-spaced peaks below  $90\text{ K}$ .<sup>40</sup> This cluster is the most conspicuous signature of the CDW phase, although it obviously raises questions of exactly how and why a singly-degenerate vibrational mode might split in a low symmetry environment. We show the behavior of the  $E_{2g}$  phonon near  $300\text{ cm}^{-1}$  for comparison. This structure hardens anharmonically with decreasing temperature but does not split across  $T_{\text{CDW}}$  - in line with the other Raman-active modes in  $\text{ScV}_6\text{Sn}_6$  including those of  $A_{1g}$  symmetry. Complementary measurements of  $\text{LuV}_6\text{Sn}_6$  and  $\text{YV}_6\text{Sn}_6$  reveal no low temperature splitting of the  $240\text{ cm}^{-1}$  mode [Supplemental figure 2], consistent with transport results indicating the absence of CDW transitions in the  $R = \text{Lu}$  and  $\text{Y}$  analogs.<sup>21,23</sup> This again demonstrates that multiplet splitting of the  $A_{1g}$  symmetry mode is a signature of the unusual CDW state in  $\text{ScV}_6\text{Sn}_6$ .

We quantify these results by fitting the Raman scattering response of  $\text{ScV}_6\text{Sn}_6$  with a series of Voigt oscillators and a linear baseline. Close-up views of the modes of interest along with their oscillator fits are shown in Fig. 2b,e. A single oscillator is required to fit the  $A_{1g}$  symmetry mode in the normal state whereas a minimum of five oscillators are needed to fit the spectra in the CDW state. By contrast, a single oscillator fits the  $E_{2g}$  mode near  $300\text{ cm}^{-1}$  over the full temperature range. The center frequency and full width at half maximum (FWHM) are extracted from these fits. The phonon lifetime  $\tau$  is a useful quantity related

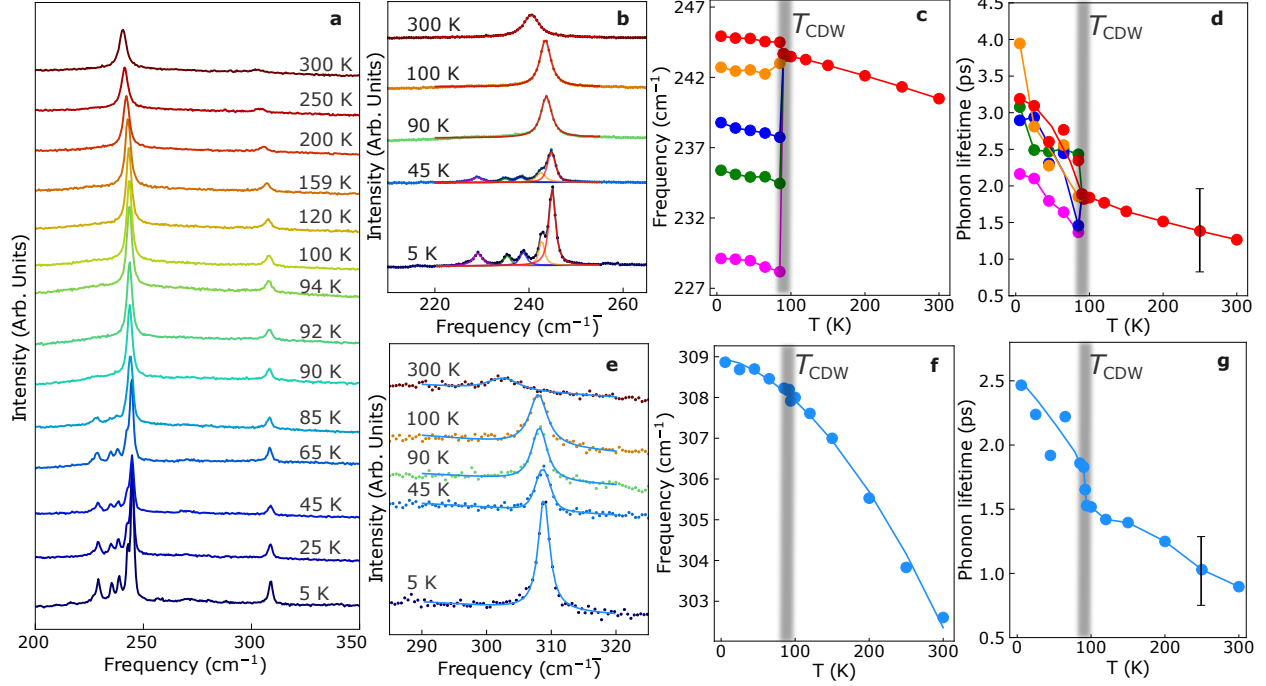


FIG. 2. **Symmetry breaking across the CDW transition in  $\text{ScV}_6\text{Sn}_6$ .** **a** Summary of the Raman-active modes near 240 and 300  $\text{cm}^{-1}$  as a function of temperature. All the spectra are collected on the  $ab$  plane in the back-scattering geometry. **b** Close-up view of the spectra at selected temperatures along with an oscillator fit. Several new features emerge in the CDW phase due to symmetry breaking. A minimum of five Voigt oscillators are needed to model the base temperature data. **c, d** Frequency vs. temperature and phonon lifetime vs. temperature trends for the features near 240  $\text{cm}^{-1}$ . These findings were extracted from the results in panel **b**. In **c**, error bars are on the order of the symbol size; a characteristic error bar is indicated in panel **d**. **e** Close-up view of the  $E_{2g}$  symmetry mode near 300  $\text{cm}^{-1}$  as a function of temperature. This mode can be fit with a single Voigt oscillator over the full temperature range. **e, f** Frequency vs. temperature and phonon lifetime vs. temperature trends for the  $E_{2g}$  symmetry mode near 300  $\text{cm}^{-1}$ . In **f**, error bars are on the order of the symbol size; a characteristic error bar is shown in panel **g**.

to the Heisenberg uncertainty principle that can be calculated as  $\tau = \hbar/\text{FWHM}$ .<sup>41</sup>

Figure 2c,d displays frequency and phonon lifetime trends as a function of temperature for the  $A_{1g}$  symmetry phonon. The sharp peak splitting immediately below  $T_{\text{CDW}}$  is consistent with a first-order phase transition,<sup>25,30–32</sup> although as we shall see below, the splitting is

not due to symmetry breaking induced splitting of components of a single mode because a singly-degenerate vibrational mode cannot not split further as part of a group-subgroup transition. At the same time, the strong clustering seems to argue against the appearance of traditional zone-folded phonons unless the phonon bands are rather flat and fold into a similar frequency window.<sup>37,42,43</sup> Overall, the phonon lifetime rises from 1.25 ps at room temperature to between 2.2 and 4 ps in the low temperature phase depending on the branch.

Figure 2f,g displays frequency and phonon lifetime of the  $E_{2g}$  phonon as a function of temperature. The mode hardening can be modeled by characteristic anharmonic effects<sup>44</sup> where  $\omega(T) = \omega_0 + A(1 + \frac{2}{e^x - 1}) + B(1 + \frac{3}{e^y - 1} + \frac{3}{(e^y - 1)^2})$  with  $x = \hbar\omega_0/2k_B T$ ,  $y = \hbar\omega_0/3k_B T$ . Here,  $\omega_0$  is the characteristic frequency at base temperature,  $A$  and  $B$  are constants. There are no anomalies in the frequency vs. temperature curve near the CDW transition. On the other hand, the phonon lifetime shows a pronounced kink at  $T_{\text{CDW}}$ , rising sharply toward a limiting low temperature value of 2.5 ps. We carried out a similar analysis of the lower frequency phonons in  $\text{ScV}_6\text{Sn}_6$  as well. No additional peak splitting or unusual phonon softening was identified within our sensitivity, although we emphasize that  $\text{ScV}_6\text{Sn}_6$  is a very low brightness sample. Thus, the dramatic peak splitting of the  $240 \text{ cm}^{-1}$   $A_{1g}$  symmetry vibrational mode is key to understanding the CDW transition.

### Phonon mixing in the low temperature phase

In order to better understand the multiplet structure of the  $240 \text{ cm}^{-1}$  phonon, we performed a symmetry analysis of the phonon modes.<sup>45</sup> In particular, we solved the *subduction* problem which relates the irreps of the high-temperature  $P6/mmm$  structure and the low-temperature  $R\bar{3}m$  structure [Table I]. This is a powerful technique that unravels a set of perturbed modes in terms of unperturbed vibrational modes.<sup>46,47</sup> As expected,  $A_{1g}$  irreps in  $P6/mmm$ , which exhibit the full crystal symmetry of the  $P6/mmm$  structure, also exhibit the full crystal symmetry of the subgroup  $R\bar{3}m$ , and thus map to  $A_{1g}$  in  $R\bar{3}m$  as well. This irrep is Raman-active in both structures, but is only one-dimensional - the single  $A_{1g}$  peak at  $240 \text{ cm}^{-1}$  in the high-temperature structure *cannot*, on its own, account for all five new modes in the  $R\bar{3}m$  structure. Where, then, do the new modes come from?

The results in Table I show that new Raman active modes can appear in  $R\bar{3}m$  from the

$B_{1g}$  modes of  $P6/mmm$  at the zone center, as well as  $P_1$  and  $P_3$  modes which fold in to  $\Gamma$  from the  $P \equiv (\frac{1}{3}, \frac{1}{3}, \frac{1}{3})$  point on the Brillouin zone boundary in reciprocal space (defined in Supplementary table S3). In order to gain a quantitative understanding of the origin of each mode, we perform an analysis where the eigenvectors of the dynamical matrix associated with each phonon mode in the  $R\bar{3}m$  structure are projected onto the eigenvectors of the dynamical matrix in the  $P6/mmm$  structure as described in the Methods section. While all symmetry-allowed  $P6/mmm$  phonon modes are allowed to mix in the formation of the  $R\bar{3}m$  phonon modes (for example, a given  $R\bar{3}m$   $A_{1g}$  mode could exhibit significant contributions from multiple  $P6/mmm$   $A_{1g}$ ,  $B_{1g}$ , and  $P_1$  modes simultaneously), this technique allows us to understand the relative magnitudes of those contributions. The results shown in Fig. 3 show eight Raman-active phonon modes in the range of  $228 \text{ cm}^{-1}$  to  $241 \text{ cm}^{-1}$  in the  $R\bar{3}m$  structure, which exhibit significant overlap with  $A_{1g}$ ,  $E_{1g}$ ,  $P_1$ , and  $P_3$  phonon modes in the range of  $220 \text{ cm}^{-1}$  to  $235 \text{ cm}^{-1}$  in the  $P6/mmm$  structure. Thus, the five clear peaks that result from the apparent splitting of the  $A_{1g}$  peak at  $240 \text{ cm}^{-1}$  observed in experiment are likely a subset of these eight modes, and therefore originate not just from the  $A_{1g}$  peak at

TABLE I. Subduction relations between the high-temperature  $P6/mmm$  and low-temperature  $R\bar{3}m$  structures. We only list the irreps of the high-symmetry structure that lead to Raman-active irreps in the low-temperature  $R\bar{3}m$  structure. Raman active irreps are highlighted in bold. For the zone-center modes, we list both the space group irrep (for example  $\Gamma_1^+$  and the corresponding point group irrep (such as  $A_{1g}$ .) Irrep labels  $P_i$  refer to irreps at the  $P \equiv (\frac{1}{3}, \frac{1}{3}, \frac{1}{3})$  point in reciprocal space for the  $P6/mmm$  structure; our definition of these irreps is included in Supplementary table S3 (our notation matches that found on the Bilbao Crystallographic Server<sup>45</sup>).

$P6/mmm$	$R\bar{3}m$
$\mathbf{A_{1g}/\Gamma_1^+} \rightarrow$	$\mathbf{A_{1g}/\Gamma_1^+}$
$B_{1g}/\Gamma_4^+ \rightarrow$	$\mathbf{A_{1g}/\Gamma_1^+}$
$\mathbf{E_{1g}/\Gamma_6^+} \rightarrow$	$\mathbf{E_g/\Gamma_3^+}$
$\mathbf{E_{2g}/\Gamma_5^+} \rightarrow$	$\mathbf{E_g/\Gamma_3^+}$
$P_1 \rightarrow$	$\Lambda_1 + \mathbf{A_{1g}/\Gamma_1^+} + A_{2u}/\Gamma_2^-$
$P_3 \rightarrow$	$\Lambda_3 + E_u/\Gamma_3^- + \mathbf{E_g/\Gamma_3^+}$

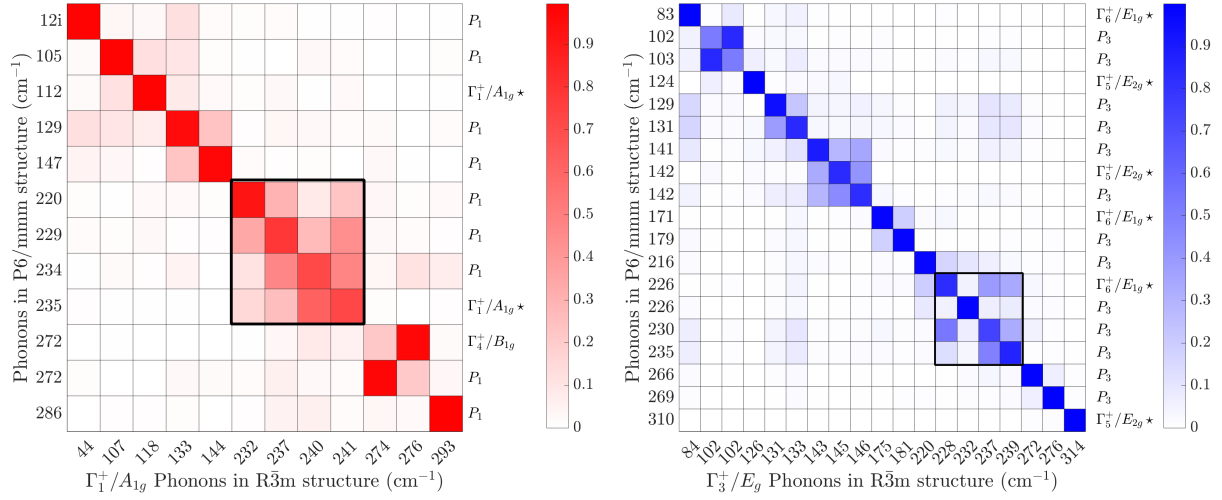


FIG. 3. Overlap of eigenvectors of the dynamical matrix between phonons in the  $P6/mmm$  structure (vertical axis) and phonons in the  $R\bar{3}m$  structure (horizontal axis). The color intensity of each box denotes the magnitude of the overlap, with a maximum possibly amplitude of unity. The lefthand panel corresponds to projections of  $P6/mmm$  phonons transforming as  $A_{1g}$ ,  $B_{1g}$ , and  $P_1$  onto  $R\bar{3}m$  phonons transforming as  $A_{1g}$ , while the righthand panel corresponds to projections of  $P6/mmm$  phonons transforming as  $E_{1g}$ ,  $E_{2g}$ , and  $P_1$  onto  $R\bar{3}m$  phonons transforming as  $E_g$ . Taken together, these two panels include all Raman-active phonon modes in the  $R\bar{3}m$  structure, as well as all  $P6/mmm$  phonon modes related to them through subduction [Table I]. Raman active modes in the  $P6/mmm$  structure are denoted with a “\*” character. In both panels, the area of interest corresponding to phonons from  $228 \text{ cm}^{-1}$  to  $241 \text{ cm}^{-1}$  in the  $R\bar{3}m$  structure are boxed. Note that the data as presented need not be symmetric.

$240 \text{ cm}^{-1}$ , but from  $E_{1g}$  modes as well as modes at the  $P$  point in reciprocal space which fold in to the  $\Gamma$  point and become Raman-active in the  $R\bar{3}m$  structure.

### Pressure destabilizes the CDW transition

Figure 4 summarizes the Raman scattering response of  $\text{ScV}_6\text{Sn}_6$  under pressure at room temperature. We focus on the behavior of the  $A_{1g}$  symmetry phonon near  $240 \text{ cm}^{-1}$  because (i) it is most strongly connected to the CDW state and (ii) all other modes show only simple hardening under compression - at least within our sensitivity. As indicated in Fig. 4a,b,

this peak can be modeled with a single oscillator below 2 GPa and also above approximately 6 GPa. At intermediate pressures, the spectra of  $\text{ScV}_6\text{Sn}_6$  are best fit with two Voigt oscillators indicating the presence of a mixed phase. This type of mixed or two-phase regime is typical for a first-order pressure-driven transition.<sup>48</sup> In this case, the mixed phase consists of  $P6/mmm$  + a new high pressure phase. Based on this behavior, we define two critical pressures:  $P_{C,1} = 2$  GPa and  $P_{C,2} = 6$  GPa.

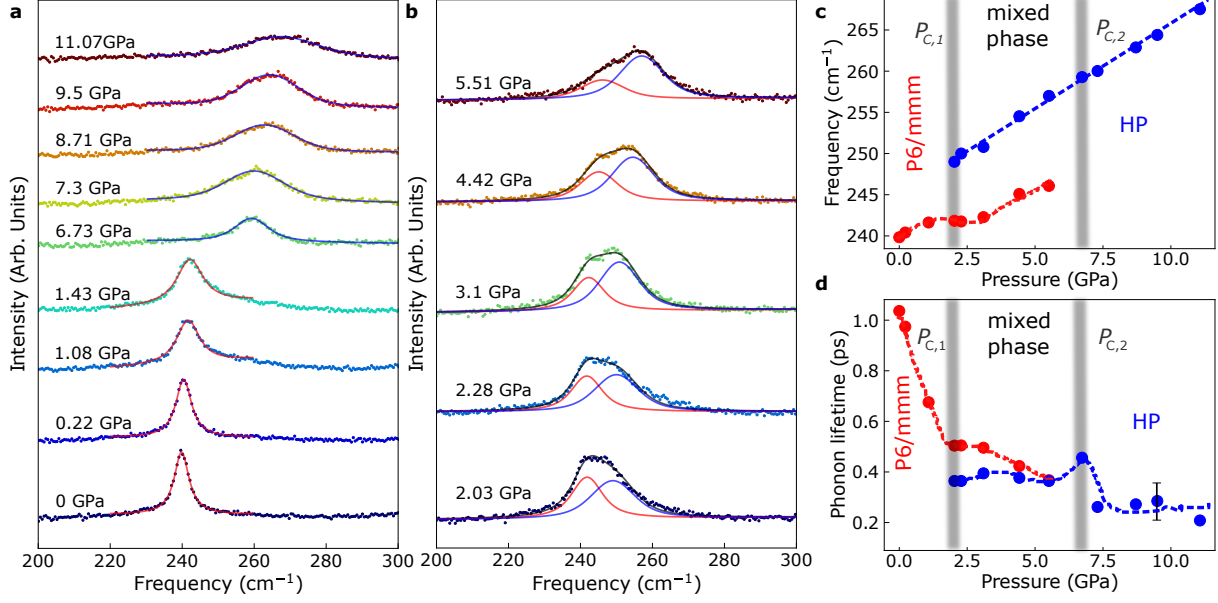


FIG. 4. **Pressure-driven structural phase transition in  $\text{ScV}_6\text{Sn}_6$  at room temperature.** **a, b** Raman scattering response as a function of pressure. The dotted lines are experimental data, and the solid lines correspond to fitted curves. **c, d** Raman shift and phonon lifetime as a function of pressure for the  $240 \text{ cm}^{-1}$  phonon. Two critical pressures ( $P_{C,1} = 2$  GPa and  $P_{C,2} = 6$  GPa) separate the  $P6/mmm$  phase, the mixed phase, and the high pressure (HP) phase. The error bars in panel **c** are on the order of the symbol size; a characteristic error bar is indicated in panel **d**.

Figure 4c,d displays frequency vs. pressure and phonon lifetime trends for  $\text{ScV}_6\text{Sn}_6$ . We find that the concentration of  $P6/mmm$  (as measured by the relative strength of the low frequency oscillator) diminishes with increasing compression in the mixed phase region whereas that of the new high pressure phase (measured by the relative strength of the second peak) increases until it dominates above  $P_{C,2}$ . The high pressure phase of  $\text{ScV}_6\text{Sn}_6$  is very similar to but not identical to  $P6/mmm$ . The single  $A_{1g}$ -like phonon mode emerging

above  $P_{C,2}$  has a higher frequency than that in the  $P6/mmm$  ground state, pointing to a stronger force constant as well as a volume reduction in the high pressure phase which may have interesting connections to the inter-layer coupling in this class of kagomé metals. At the same time, phonon lifetime drops from 1 ps at ambient pressure (lower than most traditional semiconductors and chalcogenides) to approximately 0.2 ps over this range. The decreased lifetime is due to significantly increased scattering events under compression.<sup>41</sup> We mention in passing that we could not stabilize the high pressure phase in our first principles simulations under pressure. This may be due to complications from the residual density wave state recently reported at room temperature or some other shortcoming of density functional theory.<sup>31,32</sup>

Prior transport studies reveal that the structure of  $\text{ScV}_6\text{Sn}_6$  starts to change near 2 GPa due to destabilization and disappearance of the CDW.<sup>24</sup> It is tempting to claim that this destabilization corresponds to  $P_{C,1}$ , but we must remember that our measurements are performed at room temperature - where the CDW is not fully developed. The recently reported short range CDW provides a way forward. This “residual CDW” resides in the high temperature phase of  $\text{ScV}_6\text{Sn}_6$  and hosts a  $(1/3, 1/3, 1/2)$  propagation vector.<sup>31,32</sup> We hypothesize that pressure quenches short range CDW correlations in this system as well, although it appears to do so in a first-order mixed phase manner between  $P_{C,1}$  and  $P_{C,2}$ .

There are not too many parallels between the pressure induced transition we observe here in  $\text{ScV}_6\text{Sn}_6$  and those observed in the single-layer vanadate kagomés like  $\text{AV}_3\text{Sb}_5$ , because the latter takes place at low temperature and between two different long-range-ordered CDW phases and the high symmetry phase, whereas in  $\text{ScV}_6\text{Sn}_6$  this transition takes place at room temperature, well above the long-range CDW order.<sup>49–51</sup> A possibility that explains the disappearance of CDW at high pressures is that the system undergoes a volume-collapse transition similar to those observed in the  $\text{ThCr}_2\text{Si}_2$  family of compounds, which involves the formation of Sn–Sn covalent bonds.<sup>52,53</sup> Such transitions are also observed in various iron-pnictide superconductors, and couple strongly to superconductivity because of their effect on the Fermi surface<sup>54,55</sup>. Therefore, such a transition is likely to suppress CDW as well.

Finally, we note that similar measurements on the Lu analog reveal no evidence at all for this type of pressure-induced destabilization of the short range CDW [Supplementary figure 3]. The  $A_{1g}$  symmetry mode near  $240 \text{ cm}^{-1}$  hardens systematically under compression in



line with the fact that  $\text{LuV}_6\text{Sn}_6$  does not host a CDW.<sup>56</sup> These structure-property relations are nicely unified by  $R$  site size arguments [Inset, supplementary figure 1d] which reveal that both chemical and physical pressure drive similar trends in CDW stability.

### Unraveling CDW stability in the $RV_6\text{Sn}_6$ family of materials ( $R = \text{Sc}, \text{Y}, \text{Lu}$ )

Traditionally, CDW behavior is related to a periodic lattice modulation due to Fermi surface nesting and electron-phonon interactions.<sup>57–62</sup> Unraveling the complete mechanism requires a systematic investigation of the electronic structure as well as a full exploration of the vibrational properties. In this family of materials, most of the focus so far has been on electronic properties from the point of view of electron-phonon coupling and Fermi surface nesting.<sup>38,63–66</sup> There has been significantly less effort to uncover the vibrational contribution to the development of the density wave state. This is because metallic character in both high and low temperature phases of  $\text{ScV}_6\text{Sn}_6$  prevents us from revealing the behavior of the infrared-active phonons due to screening by the Drude peak. The Raman scattering response is, however, still accessible, and combined with different external stimuli and complementary lattice dynamics calculations, a remarkable picture of phonon mixing and density wave stability is beginning to emerge.

In this work, we traced how phonons mix in the CDW state of  $\text{ScV}_6\text{Sn}_6$ , tested these ideas with symmetry arguments based upon our lattice dynamics calculations, and compared our findings to behavior in the Y and Lu analogs. Overall, we demonstrate that low temperature stabilizes the CDW whereas both physical and chemical pressures destroy it. This suggests that the coupling interactions are on the “knife’s edge”, easily manipulated by any external stimuli, and more sensitive than the similar CDW orders in the monolayer  $\text{AV}_3\text{Sb}_5$  vanadates. Our analysis reveals that the multiplet-like behavior of the  $240\text{ cm}^{-1}$  phonon in the CDW state of  $\text{ScV}_6\text{Sn}_6$  is the result of its mixing with other phonons. We emphasize that this splitting is not due to symmetry breaking of a single mode in the conventional sense. Instead, it is connected with both  $\Gamma$  and  $P$  point modes that are folded to the zone center and become Raman active, indicating that the CDW state is influenced by a variety of phonon modes and highlighting the intricate, phonon-assisted nature of the CDW state. Since the phonon mode near  $240\text{ cm}^{-1}$  also serves to connect the short-range and long-range CDWs, it provides a

sensitive, microscopic indicator of CDW stability under different tuning parameters. Finally, we point out that while prior phonon dispersion calculations emphasize the role of unstable Sn and Sc modes in the CDW state,<sup>33</sup> this and other work<sup>25,64,66</sup> is revealing that the V centers are not just spectators. Rather, the out-of-plane motion of V in the double kagomé layer is just as significant as the Sc and Sn center motion. Recent STM work reaches a similar conclusion regarding the importance of the V centers.<sup>64</sup>

## METHODS

**Crystal growth and diamond anvil cell loading:** High quality  $RV_6\text{Sn}_6$  ( $R = \text{Sc, Lu, Y}$ ) crystals were grown from a Sn-rich melt method with a composition ratio of  $R:\text{V}:\text{Sn} = 1:6:60$  as described in Ref.<sup>25</sup>. They are hexagonal blocks with clear *ab* surfaces. For the high pressure Raman scattering measurements, a small single crystal was loaded into a symmetric diamond anvil cell suitable for work in the 0 - 13 GPa range. The cell is equipped with low fluorescence diamonds with 400  $\mu\text{m}$  culets. We also employed a stainless steel gasket with a 100  $\mu\text{m}$  hole, KBr as the pressure medium, and an annealed ruby ball for pressure determination via fluorescence.<sup>67</sup>

**Raman spectroscopy:** Raman scattering measurements were performed in the back scattering geometry using a Horiba LabRAM HR Evolution spectrometer equipped with a 532 nm (green) laser, a 50 $\times$  microscope objective, 1800 line/mm gratings, and a liquid-nitrogen-cooled charge-coupled device detector. To minimize heating and maximize signal intensity for this low brightness sample, power was controlled below 7.7 mW, and the laser was slightly defocused. Each spectrum was integrated for 200 s and averaged four times. Variable temperature work was carried out with a low-profile open-flow cryostat, and high pressure measurements employed a diamond anvil cell as described above. Standard peak fitting techniques were employed as appropriate.

**Lattice dynamics calculations:** All density functional theory (DFT) calculations were performed with Projector Augmented Waves (PAW) as implemented in the Vienna Ab initio simulation package (VASP) version 5.4.4<sup>68-70</sup> using the PBEsol exchange-correlation functional for valence configurations of Sc, V, and Sn corresponding to  $3s^23p^64s^13d^2$ ,  $3s^23p^64s^13d^4$ , and  $5s^24d^{10}5p^2$ , respectively. Unless otherwise mentioned, experimentally

determined lattice parameters of  $a = 5.475 \text{ \AA}$  and  $c = 9.177 \text{ \AA}$  for the  $P6/mmm$  structure and  $a = 9.456 \text{ \AA}$  and  $c = 27.412 \text{ \AA}$  for the conventional  $R\bar{3}m$  structure were used for all calculations. Internal degrees of freedom were relaxed, with forces converged to within  $0.001 \text{ eV/\AA}$  using a plane wave cutoff energy of  $400 \text{ eV}$ , combined with a  $\Gamma$ -centered Monkhorst-Pack k-point mesh of  $20 \times 20 \times 10$  in the  $P6/mmm$  structure, as well as a Gaussian smearing parameter of  $10 \text{ meV}$ . Calculations in the  $R\bar{3}m$  structure were carried out in a primitive, three formula-unit cell commensurate with the wavevector  $P = (\frac{1}{3}, \frac{1}{3}, -\frac{1}{3})$ , which corresponds to a unit cell with basis vectors  $(\frac{2}{3}, \frac{1}{3}, \frac{1}{3}), (-\frac{1}{3}, \frac{1}{3}, \frac{1}{3}), (-\frac{1}{3}, -\frac{2}{3}, \frac{1}{3})$ , where the indices  $(a, b, c)$  correspond to the lattice vectors of the conventional  $R\bar{3}m$  nine formula unit cell. All computational parameters used for this structure were the same as for the  $P6/mmm$  structure, except with a  $\Gamma$ -centered Monkhorst-Pack k-point mesh of  $10 \times 10 \times 10$ . To calculate phonon frequencies and their associated distortions, we constructed the dynamical matrix in a basis of symmetry adapted modes, which bring the dynamical matrix into block diagonal form, where each block corresponds to a single irreducible representation of the space group. These symmetry-adapted linear combinations of atomic displacements were found using the ISOTROPY software suite.<sup>71</sup>

**Phonon overlap:** After calculating the eigenvectors of the dynamical matrix associated with each phonon mode, we then computed the relationship between eigenvectors  $\hat{e}_i^{I\alpha}$  in the  $P6/mmm$  structure (where  $I$  is an irrep,  $\alpha$  the mode index within that irrep, and  $i$  the ionic degree of freedom in cartesian coordinates), and the eigenvectors  $\hat{g}_i^{I\alpha}$  in the  $R\bar{3}m$  structure. First, the  $\hat{e}_i^{I\alpha}$  were expressed in a three formula unit basis commensurate with the  $R\bar{3}m$  cell, then renormalized. The overlap for two phonons is then defined as the projection of  $\hat{g}_i^{I\alpha}$  onto  $\hat{e}_i^{I\alpha}$ ,

$$O(J, \beta, I, \alpha) = \sqrt{\left(\hat{g}_i^{J\beta} \hat{e}_i^{I\alpha}\right)^2}. \quad (1)$$

In the lefthand panel of Fig. 3,  $J = A_{1g}$ , and  $I \in A_{1g}, B_{1g}, P_1$ , as determined by the solution to the subduction problem described in Table I. In the righthand panel,  $J = E_g$ , and  $I \in E_{1g}, E_{2g}, P_3$ . In this second case, the  $E_{1g}$  and  $E_{2g}$  phonons are doubly degenerate, and the  $P_3$  phonons quadruply degenerate. In order to compress the results of the table, instead of reporting a cell for each individual degenerate mode, our figure includes a single cell with

amplitude defined as  $\tilde{O}$ , where

$$\tilde{O}(J, \beta, I, \alpha) \equiv \frac{1}{M_\beta} \sum_{\beta_l} \sqrt{\sum_{\alpha_m} O(J, \beta_l, I, \alpha_m)^2}. \quad (2)$$

Here,  $l$  and  $m$  run over the degenerate indices of  $\beta$  and  $\alpha$  respectively, and  $M_\beta$  is the multiplicity of the  $\beta$  irrep being projected. Similar approaches have been employed in other materials.<sup>46,47</sup>

**Group Theory:** The symmetry-adapted linear combinations of atomic displacements used for the phonon calculations were found using the ISOTROPY software suite.<sup>71</sup> The subduction analysis to find the connections between irreps through the group-subgroup transition was performed using the CORREL application hosted by the Bilbao crystallographic server.<sup>45</sup>

## DATA AVAILABILITY

Data are available from the corresponding authors upon reasonable request.

## ACKNOWLEDGEMENTS

Work at Tennessee (YG, KAS, ALB, and JLM) is supported by Physical Behavior of Materials, Basic Energy Sciences, U.S. Department of Energy (Contract number DE-SC00023144). DM and WRM acknowledges funding from the Gordon and Betty Moore Foundation’s EPiQS Initiative, Grant GBMF9069. Work at the University of Minnesota (ETR and TB) was supported by NSF CAREER grant DMR-2046020.

## AUTHOR CONTRIBUTIONS

YG and JLM designed the study. WRM, SM, and RPM grew the crystals with guidance from DGM. ALB carried out feasibility measurements while YG performed the variable temperature and high pressure Raman scattering spectroscopy. ER performed the theoretical calculations and discussed the results with TB. YG and KAS analysed the spectral data with

guidance from JLM. YG, ER, and JLM wrote the manuscript. All authors commented on the text.

## COMPETING INTERESTS

The authors declare no competing financial or non-financial interests.

- 
- [1] Kang, M. *et al.* Dirac fermions and flat bands in the ideal kagome metal FeSn. *Nature materials* **19**, 163–169 (2020).
  - [2] Li, M. *et al.* Dirac cone, flat band and saddle point in kagome magnet YMn<sub>6</sub>Sn<sub>6</sub>. *Nature communications* **12**, 3129 (2021).
  - [3] Liu, Z. *et al.* Orbital-selective Dirac fermions and extremely flat bands in frustrated kagome-lattice metal CoSn. *Nature communications* **11**, 4002 (2020).
  - [4] Yin, J.-X. *et al.* Negative flat band magnetism in a spin–orbit-coupled correlated kagome magnet. *Nature Physics* **15**, 443–448 (2019).
  - [5] Balents, L. Spin liquids in frustrated magnets. *Nature* **464**, 199–208 (2010).
  - [6] Yan, S., Huse, D. A. & White, S. R. Spin-liquid ground state of the S= 1/2 kagome Heisenberg antiferromagnet. *Science* **332**, 1173–1176 (2011).
  - [7] Meier, W. R. *et al.* Flat bands in the CoSn-type compounds. *Phys. Rev. B* **102**, 075148 (2020).
  - [8] Paul, A., Chung, C.-M., Birol, T. & Changlani, H. J. Spin-lattice Coupling and the Emergence of the Trimerized Phase in the S= 1 Kagome Antiferromagnet Na<sub>2</sub>Ti<sub>3</sub>Cl<sub>8</sub>. *Phys. Rev. Lett.* **124**, 167203 (2020).
  - [9] Ye, L. *et al.* Massive Dirac fermions in a ferromagnetic kagome metal. *Nature* **555**, 638–642 (2018).
  - [10] Lachman, E. *et al.* Exchange biased anomalous Hall effect driven by frustration in a magnetic kagome lattice. *Nature communications* **11**, 560 (2020).
  - [11] Tanaka, M. *et al.* Topological Kagome magnet Co<sub>3</sub>Sn<sub>2</sub>S<sub>2</sub> thin flakes with high electron mobility and large anomalous Hall effect. *Nano Lett.* **20**, 7476–7481 (2020).

- [12] Xu, G., Lian, B. & Zhang, S.-C. Intrinsic quantum anomalous hall effect in the kagome lattice  $\text{Cs}_2\text{LiMn}_3\text{F}_{12}$ . *Phys. Rev. Lett.* **115**, 186802 (2015).
- [13] Rüegg, A. & Fiete, G. A. Fractionally charged topological point defects on the kagome lattice. *Phys. Rev. B* **83**, 165118 (2011).
- [14] Feng, Z. *et al.* Gapped spin-1/2 spinon excitations in a new kagome quantum spin liquid compound  $\text{Cu}_3\text{Zn}(\text{OH})_6\text{FBr}$ . *Chinese Physics Letters* **34**, 077502 (2017).
- [15] Ghimire, N. J. *et al.* Competing magnetic phases and fluctuation-driven scalar spin chirality in the kagome metal  $\text{YMn}_6\text{Sn}_6$ . *Science Advances* **6**, eabe2680 (2020).
- [16] Wang, Q. *et al.* Field-induced topological Hall effect and double-fan spin structure with a  $c$ -axis component in the metallic kagome antiferromagnetic compound  $\text{YMn}_6\text{Sn}_6$ . *Phys. Rev. B* **103**, 014416 (2021).
- [17] Teng, X. *et al.* Magnetism and charge density wave order in kagome  $\text{FeGe}$ . *Nature Physics* 1–9 (2023).
- [18] Ortiz, B. R. *et al.* New kagome prototype materials: discovery of  $\text{KV}_3\text{Sb}_5$ ,  $\text{RbV}_3\text{Sb}_5$ , and  $\text{CsV}_3\text{Sb}_5$ . *Phys. Rev. Mater.* **3**, 094407 (2019).
- [19] Ortiz, B. R. *et al.*  $\text{CsV}_3\text{Sb}_5$ : A  $\mathbb{Z}_2$  topological kagome metal with a superconducting ground state. *Phys. Rev. Lett.* **125**, 247002 (2020).
- [20] Teng, X. *et al.* Discovery of charge density wave in a kagome lattice antiferromagnet. *Nature* **609**, 490–495 (2022).
- [21] Pokharel, G. *et al.* Electronic properties of the topological kagome metals  $\text{YV}_6\text{Sn}_6$  and  $\text{GdV}_6\text{Sn}_6$ . *Phys. Rev. B* **104**, 235139 (2021).
- [22] Hu, Y. *et al.* Tunable topological Dirac surface states and van Hove singularities in kagome metal  $\text{GdV}_6\text{Sn}_6$ . *Science Advances* **8**, eadd2024 (2022).
- [23] Zhang, X. *et al.* Electronic and magnetic properties of intermetallic kagome magnets  $\text{RV}_6\text{Sn}_6$  ( $R = \text{Tb}–\text{Tm}$ ). *Phys. Rev. Mater.* **6**, 105001 (2022).
- [24] Zhang, X. *et al.* Destabilization of the charge density wave and the absence of superconductivity in  $\text{ScV}_6\text{Sn}_6$  under high pressures up to 11 GPa. *Materials* **15**, 7372 (2022).
- [25] Arachchige, H. W. S. *et al.* Charge density wave in kagome lattice intermetallic  $\text{ScV}_6\text{Sn}_6$ . *Phys. Rev. Lett.* **129**, 216402 (2022).

- [26] Ritz, E. T. *et al.* Orbital-selective electron-phonon coupling and superconductivity in  $\text{av}_3\text{sb}_5$ . *arXiv preprint arXiv:2304.14822* (2023).
- [27] Zhao, H. *et al.* Cascade of correlated electron states in the kagome superconductor  $\text{CsV}_3\text{Sb}_5$ . *Nature* **599**, 216–221 (2021).
- [28] Liang, Z. *et al.* Three-dimensional charge density wave and surface-dependent vortex-core states in a kagome superconductor  $\text{CsV}_3\text{Sb}_5$ . *Phys. Rev. X* **11**, 031026 (2021).
- [29] Du, F. *et al.* Pressure-induced double superconducting domes and charge instability in the kagome metal  $\text{KV}_3\text{Sb}_5$ . *Phys. Rev. B* **103**, L220504 (2021).
- [30] Hu, T. *et al.* Optical spectroscopy and band structure calculations of the structural phase transition in the vanadium-based kagome metal  $\text{ScV}_6\text{Sn}_6$ . *Phys. Rev. B* **107**, 165119 (2023).
- [31] Cao, S. *et al.* Competing charge-density wave instabilities in the kagome metal  $\text{ScV}_6\text{Sn}_6$ . *arXiv preprint arXiv:2304.08197* (2023).
- [32] Korshunov, A. *et al.* Softening of a flat phonon mode in the kagome  $\text{ScV}_6\text{Sn}_6$ . *arXiv preprint arXiv:2304.09173* (2023).
- [33] Tan, H. & Yan, B. Abundant lattice instability in kagome metal  $\text{ScV}_6\text{Sn}_6$ . *arXiv preprint arXiv:2302.07922* (2023).
- [34] Fan, S. *et al.* Electronic chirality in the metallic ferromagnet  $\text{Fe}_{1/3}\text{TaS}_2$ . *Phys. Rev. B* **96**, 205119 (2017).
- [35] Fan, S. *et al.* Excitations of intercalated metal monolayers in transition metal dichalcogenides. *Nano Lett.* **21**, 99–106 (2020).
- [36] Wu, S. *et al.* Charge density wave order in the kagome metal  $\text{AV}_3\text{Sb}_5$  ( $A = \text{Cs}, \text{Rb}, \text{K}$ ). *Phys. Rev. B* **105**, 155106 (2022).
- [37] Liu, G. *et al.* Observation of anomalous amplitude modes in the kagome metal  $\text{CsV}_3\text{Sb}_5$ . *Nature communications* **13**, 3461 (2022).
- [38] Hu, Y. *et al.* Phonon promoted charge density wave in topological kagome metal  $\text{ScV}_6\text{Sn}_6$ . *arXiv preprint arXiv:2304.06431* (2023).
- [39] Ohno, H., Iizuka, Y. & Fujita, S. Pure rotational raman spectroscopy applied to  $\text{N}_2/\text{O}_2$  analysis of air bubbles in polar firn. *Journal of Glaciology* **67**, 903–908 (2021).
- [40] The low brightness of this sample and resolution issues make it difficult to tell whether the small shoulders and tiny features on the baseline are real - sufficiently different from nearby

peaks as well as the noise level.

- [41] Sun, Q.-C. *et al.* Spectroscopic determination of phonon lifetimes in rhenium-doped MoS<sub>2</sub> nanoparticles. *Nano Lett.* **13**, 2803–2808 (2013).
- [42] Joshi, J. *et al.* Short-range charge density wave order in 2H–TaS<sub>2</sub>. *Phys. Rev. B* **99**, 245144 (2019).
- [43] Hill, H. M. *et al.* Phonon origin and lattice evolution in charge density wave states. *Phys. Rev. B* **99**, 174110 (2019).
- [44] Balkanski, M., Wallis, R. F. & Haro, E. Anharmonic effects in light scattering due to optical phonons in silicon. *Phys. Rev. B* **28**, 1928–1934 (1983).
- [45] Aroyo, M. I., Kirov, A., Capillas, C., Perez-Mato, J. & Wondratschek, H. Bilbao Crystallographic Server. II. Representations of crystallographic point groups and space groups. *Acta Crystallographica Section A: Foundations of Crystallography* **62**, 115–128 (2006).
- [46] Long, V. C. *et al.* Far-infrared vibrational properties of high-pressure high-temperature C<sub>60</sub> polymers and the C<sub>60</sub> dimer. *Phys. Rev. B* **61**, 13191–13201 (2000).
- [47] Zhu, Z.-T. *et al.* Far-infrared vibrational properties of tetragonal C<sub>60</sub> polymer. *Phys. Rev. B* **65**, 085413 (2002).
- [48] Musfeldt, J., Mandrus, D. & Liu, Z. Insulator–metal transition in CrSiTe<sub>3</sub> triggered by structural distortion under pressure. *npj 2D Materials and Applications* **7**, 28 (2023).
- [49] Zhang, Z. *et al.* Pressure-induced reemergence of superconductivity in the topological kagome metal CsV<sub>3</sub>Sb<sub>5</sub>. *Phys. Rev. B* **103**, 224513 (2021).
- [50] Gupta, R. *et al.* Two types of charge order with distinct interplay with superconductivity in the kagome material CsV<sub>3</sub>Sb<sub>5</sub>. *Communications Physics* **5**, 232 (2022).
- [51] Ritz, E. T., Fernandes, R. M. & Birol, T. Impact of Sb degrees of freedom on the charge density wave phase diagram of the kagome metal CsV<sub>3</sub>Sb<sub>5</sub>. *arXiv preprint arXiv:2212.13319* (2022).
- [52] Hoffmann, R. & Zheng, C. Making and breaking bonds in the solid state: The ThCr<sub>2</sub>Si<sub>2</sub> structure. *The Journal of Physical Chemistry* **89**, 4175–4181 (2002).
- [53] Foroozani, N. *et al.* Hydrostatic high-pressure studies to 25 GPa on the model superconducting pnictide LaRu<sub>2</sub>P<sub>2</sub>. In *Journal of Physics: Conference Series*, vol. 500, 032007 (IOP Publishing, 2014).



- [54] Kreyssig, A. *et al.* Pressure-induced volume-collapsed tetragonal phase of  $\text{CaFe}_2\text{As}_2$  as seen via neutron scattering. *Phys. Rev. B* **78**, 184517 (2008). URL <https://link.aps.org/doi/10.1103/PhysRevB.78.184517>.
- [55] Saha, S. *et al.* Structural collapse and superconductivity in rare-earth-doped  $\text{CaFe}_2\text{As}_2$ . *Phys. Rev. B* **85**, 024525 (2012).
- [56] Lee, J. & Mun, E. Anisotropic magnetic property of single crystals  $\text{RV}_6\text{Sn}_6$  ( $R = \text{Y, Gd-Tm, Lu}$ ). *Phys. Rev. Mater.* **6**, 083401 (2022).
- [57] Zhu, X., Cao, Y., Zhang, J., Plummer, E. & Guo, J. Classification of charge density waves based on their nature. *Proceedings of the National Academy of Sciences* **112**, 2367–2371 (2015).
- [58] Grüner, G. & Zettl, A. Charge density wave conduction: A novel collective transport phenomenon in solids. *Physics Reports* **119**, 117–232 (1985).
- [59] Roy, A. P., Bajaj, N., Mittal, R., Babu, P. D. & Bansal, D. Quasi-One-Dimensional Fermi Surface Nesting and Hidden Nesting Enable Multiple Kohn Anomalies in  $\alpha$ -Uranium. *Phys. Rev. Lett.* **126**, 096401 (2021).
- [60] Brouet, V. *et al.* Fermi Surface Reconstruction in the CDW State of  $\text{CeTe}_3$  Observed by Photoemission. *Phys. Rev. Lett.* **93**, 126405 (2004).
- [61] Weber, F. *et al.* Electron-phonon coupling and the soft phonon mode in  $\text{TiSe}_2$ . *Phys. Rev. Lett.* **107**, 266401 (2011).
- [62] Jurczek, E. & Rice, T. A charge-density-wave instability in  $\text{BaBi}_{1-x}\text{Pb}_x\text{O}_3$  caused by strong electron-phonon coupling. *Europhysics Letters* **1**, 225 (1986).
- [63] Lee, S. *et al.* Nature of charge density wave in kagome metal  $\text{ScV}_6\text{Sn}_6$  (2023). 2304.11820.
- [64] Cheng, S. *et al.* Nanoscale visualization and spectral fingerprints of the charge order in  $\text{ScV}_6\text{Sn}_6$  distinct from other kagome metals. *arXiv preprint arXiv:2302.12227* (2023).
- [65] Kang, S.-H. *et al.* Emergence of a new band and the Lifshitz transition in kagome metal  $\text{ScV}_6\text{Sn}_6$  with charge density wave. *arXiv preprint arXiv:2302.14041* (2023).
- [66] Tuniz, M. *et al.* Dynamics and resilience of the charge density wave in a bilayer kagome metal. *arXiv preprint arXiv:2302.10699* (2023).
- [67] Mao, H., Bell, P., Shaner, J. t. & Steinberg, D. Specific volume measurements of Cu, Mo, Pd, and Ag and calibration of the ruby R1 fluorescence pressure gauge from 0.06 to 1 Mbar. *Journal of applied physics* **49**, 3276–3283 (1978).

- [68] Kresse, G. & Hafner, J. Ab initio molecular dynamics for liquid metals. *Phys. Rev. B* **47**, 558 (1993).
- [69] Kresse, G. & Furthmüller, J. Efficiency of ab-initio total energy calculations for metals and semiconductors using a plane-wave basis set. *Comput. Mater. Sci.* **6**, 15–50 (1996).
- [70] Kresse, G. & Furthmüller, J. Efficient iterative schemes for ab initio total-energy calculations using a plane-wave basis set. *Phys. Rev. B* **54**, 11169 (1996).
- [71] Stokes, H., Hatch, D. & Campbell, B. ISOTROPY Software Suite v. 9.6.1. *iso.byu.edu* (2022).
- [72] Johannes, M. D. & Mazin, I. I. Fermi surface nesting and the origin of charge density waves in metals. *Phys. Rev. B* **77**, 165135 (2008).
- [73] Hoesch, M., Bosak, A., Chernyshov, D., Berger, H. & Krisch, M. Giant Kohn Anomaly and the Phase Transition in Charge Density Wave  $\text{ZrTe}_3$ . *Phys. Rev. Lett.* **102**, 086402 (2009).
- [74] Varma, C. M. & Simons, A. L. Strong-Coupling Theory of Charge-Density-Wave Transitions. *Phys. Rev. Lett.* **51**, 138–141 (1983).